

Low-temperature tunneling of CH₃ quantum rotor in van der Waals solids

Nikolas P. Benetis¹, Ilia A. Zelenetckii², and Yuriy A. Dmitriev³

¹*Department of Environmental Engineering and Antipollution Control, Technological Educational Institute of Western Macedonia (TEI), Kila 50 100 Kozani, Greece*

²*Department of System Analysis and Control, Institute of Computer Science and Technology, Peter the Great St. Petersburg Polytechnic University, 29 Politekhnikeskaya ul., St. Petersburg 195251, Russia*

³*Ioffe Institute, 26 Politekhnikeskaya ul., St. Petersburg 194021, Russia*

E-mail: niben@eie.gr

Received July 30, 2018, published online February 25, 2019

Motional quantum effects of tunneling methyl radical isolated in solid gases as they appear on experimental electron paramagnetic resonance (EPR) spectra are examined. Obtained analytical expressions of the tunneling frequency for methyl rotor/torsional-oscillator utilizing localized Hermite polynomials are compared to full numerical computations and tested against experimental EPR lineshape simulations. In particular, the X-band of methyl radical was displaying partial anisotropy averaging even at lowest temperatures. EPR lineshape simulations involving rotational dynamics were applied for the accurate determination of the potential barrier and the tunneling frequency. Tunneling frequency, as the splitting between the *A* and *E* torsional levels by the presence of a periodic *C*₃ model potential with periodic boundary conditions, was computed and related to the EPR-lineshape alteration. The corresponding *C*₂ rotary tunneling about the in-plane axes of methyl was also studied while both the *C*₂ and *C*₃ rotations were compared with the rotation of deuteriated methyl radical.

Keywords: solid gases, methyl rotary tunneling, analytical tunneling frequency, tunnel frequency vs. hindering barrier.

1. Introduction

A vast number of processes in solid state are realized through potential-barrier hindering dynamics of hosted neutral or charged particles/probes. For example, at low temperatures, the only way for a particle to overcome a potential barrier is by quantum tunneling which becomes crucially enhanced for light atoms and molecules. Among those, methyl radical (CH₃ and its isotope analogues) is considered as quantum rotator because of its small inertia. The radical may be stabilized in chemically inert matrices of which cryocrystals are of particular interest. Monoatomic examples of host matrices are Ne, Ar, Kr, Xe, while molecular-gas host matrices of general cryogenic interest are hydrogen H₂, nitrogen N₂, oxygen O₂, carbon monoxide CO, carbon dioxide CO₂, nitrous oxide N₂O and methane CH₄. The rotational behavior of methyl radical embedded in these matrices is very sensitive to the state and dynamics of the surrounding matrix molecules. Therefore, electron paramagnetic resonance (EPR) which provides information on such phenom-

ena is a good tool to study the solid state behavior of such embedded radicals at very low temperature.

The molecules of cryocrystals are held together by weak van der Waals forces and are among the simplest solids to test *ab initio* theoretical approaches. However, even in these solids, composed of most weakly bounded particles, the interactions contributing to the energy of the matrix particles may reach rather high values. For example, the central attraction energy of a matrix molecule in solid CO₂ is of the order of 10787 cal/mole [1] which is equivalent to 5428.3 K. The rotational tunneling and librations of the matrix isolated CH₃ radical are, thus, the major mechanisms of the radical reorientation at the cryogenic temperatures. The reorientational motion of CH₃ in molecular cryocrystals was found to be complex in nature and included fast rotation around the molecular *C*₃ axis, fast librations around the in-plane *C*₂ axis, and slow tunneling tumbling about *C*₂ axis [2–4]. The observed temperature dependence of methyl radical motion in these previous studies clearly evidences specific changes occurring in the orientation dynamics of the matrix mole-

cules. The results are in line with a very recent study [5] by Krainyukova and Kuchta who reported new insight on the molecular structure and dynamics of solid CO₂. These authors performed a high-energy electron diffraction study on solid carbon dioxide films in the temperature range 15–87 K and found hopping precession of molecules instead of simple small-angle librations that should not exceed 5–6 degrees. The relevant maximal angle deviations turned out to be as big as ~30 deg at the lowest temperatures (~15 K) and started to decrease with rise in temperature at ~45 K. This temperature point almost exactly coincides with the onset of the anisotropic C₂ rotation we observed in our methyl radical EPR study in solid CO₂ [4]. It is worth noting that, earlier, the rank-4 orientational order parameter η₄ was found to decrease rapidly in pure solid CO₂ at temperatures above 45 K [6]. This η₄ parameter determines the correlative and rotational-unharmonic effects in the librational subsystem. In fact, EPR studies of CH₃ stabilized in solid Kr films discovered formation of a highly disordered matrix structure for samples condensed from the gas phase at 4.2 K [7] as well as 16 K [8]. The structure accumulated the majority of trapped radicals which survived annealing to 31 K [8]. The radicals in the disordered structure yielded very broad hyperfine (*hf*) lines compared to those at the centers in the symmetric substitutional sites of the regular Kr lattice. The broadening was found to originate from the distribution of the radical *g*-factor due to the matrix effect. An attempt of assessing the disorder parameter was presented in Ref. 3.

The present study is aimed at elucidating matrix effects in rotationally averaged methyl radical parameters and correlating tunneling rates to barriers of rotation for CH₃ in van der Waals solids. The results are essential for converting the radical to a probe to determine low-temperature structures and dynamics processes occurring in cryocrystals.

An estimation of the tunneling particle mobility is possible through the tunneling frequency [9] which can be used identically as the torsional splitting of the localized degenerate vibrators' ground level. The torsional splitting is thus per definition a temperature independent quantity as it requires an isolated quantum system. Experimentally, the torsional splitting is observable at lowest temperature while the definition of the tunneling frequency ν_t is given differently by Stejskal and Gutowsky [10]:

$$\nu_t = \frac{1}{Q} \sum_i \nu_i e^{-\bar{E}_i/RT}. \quad (1)$$

The average energies \bar{E}_i of each originally two-fold degenerate localized torsional level, *i*, (C₂ potential was assumed in that work), in the above Eq. (1) weights the corresponding torsional splitting ν_i . The partition function *Q*, comprising the sum of the Boltzmann exponentials, is the normalization factor. The Boltzmann statistics used to obtain the populations of the torsional levels thus renders the

above “tunneling frequency” ν_t as temperature-dependent function.

There is, however, a fundamental drawback for the usefulness of the definition in Eq. (1) in quantum systems; in particular, for large potentials of the order of 1000 K and higher. The difference in the energies of the torsional levels is too large to give any significant population to any other levels than the ground level.

In many other systems of tunneling methyl radical, similar to our case, a simple estimation gives the observable effect from the higher torsional levels for temperatures higher than 250 K, while experimentally, the importance of the motional quantum effects become secondary for temperature higher than 50 K. In this estimation the torsional energies $E_v = 3(BV_3)^{1/2}(v + 1/2)$ were used, *vide infra*, for rotational energy *B* ca 7 K and potential barriers $V_3 = 1000$ K. Notice also that barriers over 1200 K studied by Stejskal and Gutowsky [10] were exceedingly larger than the one used in the latter estimation and the ones of interest in the present work.

Following the above discussion, we simplify our calculations by not incorporating higher torsional levels than the ground level as also explained by Yamada *et al.* [11]. Further details of this approximation are discussed in the section about the theory of the tunneling-methyl radical. The general quantum mechanical problem of tunneling for hindering potentials of C₃ and C₂ symmetries are also treated easily in the present work within a numerical formalism. The applied method is also applicable for potentials of arbitrary complexity provided that its matrix elements in the simple Bloch-type basis set are available.

The article is organized as follows: In Sec. 2, the experimental matrix shift of the EPR parameters and the anisotropy of methyl, CH₃, radical isolated in four different matrices consisting of spherical molecules are analyzed in relation to the radical tunneling frequencies at cryogenic temperatures. The role of librations in the averaging of the parameter anisotropies is also considered for slightly higher temperatures where quantum and classical motion coexist. The results are utilized in Secs. 3 and 4 to theoretically address the rotational rates and the libration amplitudes of the trapped methyl radicals even in matrices consisting of linear molecules. In particular, the tunneling frequencies of methyl radical against periodic C₃ or C₂ hindering potentials are computed both analytically and numerically exploiting the experimental EPR results. The EPR results correspond, respectively, to parallel or perpendicular rotary tunneling motions of methyl radical in different solid gas matrices, concerning exclusively very low-temperature quantum conditions. The main task is to show that a wealth of perceptible orientational motions is available for a 3D quantum rotator even at cryogenic temperatures by tunneling through barriers. Finally, after a short concluding Sec. 5, an Appendix demonstrating the mathematical details of the computations is included.

2. Hindered molecular rotation effect on the EPR parameters

The EPR lineshape of CH₃ trapped in van der Waals (vdW) solids at cryogenic temperatures demonstrates significant variability. It changes from nearly symmetric for methyl radical in solid *p*-H₂ [12], to asymmetric spectrum with split anisotropic lines and additional satellite transitions of non-rotating methyls, in cold solids consisting of the linear CO₂, N₂O molecules. The above two sets of main and additional transitions are characterized by either isotropic or axial spin-Hamiltonian vs. rhombic spin-Hamiltonian, respectively [13,14], depending on the actual dispersion forces between matrix and CH₃ radicals [15]. The experimental anisotropy variation of the EPR spectra of methyl radical in the present work was related to increasing rotational rate of the radical with temperature increase. The variation of the radical-matrix interaction influences the matrix shifts of the EPR parameters and changes the radical dynamics governing the parameter averaging. Moreover, it is not possible to determine the exact static anisotropy of the **g** and **A** tensors experimentally, since methyl tunnels (rotates) even at the lowest experimental temperatures.

Radical species isolated in a matrix cage are allowed to perform orientational and/or oscillatory motions. In case of a weak matrix coupling, the trapped molecules rotate almost freely in the host cage, yielding nearly isotropic EPR parameters with small matrix shifts. Free rotation quantum effects at 4.2 K were observed early by Foner *et al.* [16] in the EPR experiments of NH₂ radical. These effects were further explained by McConnell [17] who also foresaw the liquid He 1:1:1:1 methyl quartet. Extending the same basic considerations, high-resolution EPR spectra with obvious Pauli excluded EPR transitions of methyl hydrogen isotopomers were observed experimentally in cryogenic Ar matrix and interpreted accordingly [11]. Matrix effects of CH₃ in solid gases of spherical particles, in particular, spectrum anisotropy, were studied semiquantitatively in [12], setting the following empirical coefficient, A_{rel} , as its measure:

$$A_{\text{rel}} = \left(\sqrt{\frac{A_{0\text{max}}}{A_{0\text{min}}}} - 1 \right) / \left(\sqrt{\frac{A_{0\text{max}}}{A_{0\text{min}}}} + 1 \right). \quad (2)$$

In Eq. (2), $A_{0\text{max}}$ and $A_{0\text{min}}$ are the amplitudes of the strongest and weakest hyperfine (hf) components of the EPR quartet. It was shown that the anisotropy was governed mainly by short-range Pauli exclusion forces while the contribution of the van der Waals attraction was negligible. Varying amplitudes and widths of the different hf components indicate residual magnetic anisotropy due to incomplete rotational averaging of the spectral parameters. Below the liquid helium temperature methyl radicals are in the ground rotation *A*-symmetry state yielding axially symmetric **g** and **A** hf tensors with parallel component coinciding with the

highest *C*₃ symmetry axis of the radical [13]. The spectrum averaging is achieved by additional fast rotation about the in-plane axes (perpendicular rotation). The rotation is characterized by tunneling frequency estimated as the reciprocal of the rotation correlation time, τ_{corr} , considered as measure of rotation hindrance. One of the aims of the present study is to verify the exclusive effect of the Pauli interaction on the spectrum anisotropy and obtain information about the CH₃ rotation dynamics by measuring and correlating τ_{corr} to the radical-matrix interaction.

First, we address the case of methyl radical in solid Ar; at 4.2 K, the spectrum of solid Ar is composed of four hf lines with different amplitudes, *A*, and widths, ΔH [18]. The line intensities, estimated as the products $A(\Delta H)^2$ are nearly equal yielding the well-known 1:1:1:1 low-temperature intensity ratio. The different widths and amplitudes of the four components are due to the residual anisotropy after partial rotational averaging. In Fig. 1(a), the reciprocal square roots of the hf amplitudes, $1/\sqrt{A}$ are proportional to the line width [12] that may be approximated by the following quadratic in m_F formula [19]:

$$\frac{1}{\sqrt{A}} \propto \Delta H = a + b m_F + c m_F^2. \quad (3)$$

Here, m_F is the projection of the coupled nuclear spin representation $\mathbf{F} = \mathbf{I}_1 + \mathbf{I}_2 + \mathbf{I}_3$ of the three protons.

The procedure of obtaining the CH₃ EPR parameters and rotation correlation times was divided into two steps as follows: First, the experimental reciprocal square root amplitudes of the hf components in Figs. 1(a)–(d) were fitted by adjusting the coefficients *a*, *b* and *c* of Eq. (3) assuming fast-motion regime conditions. The Origin 6.1 routine was used to determine the polynomial coefficients minimizing the standard deviation (SD) of the best curve fit through the experimental data.

The EPR parameters were obtained from the above fitting procedure using reasonable estimates of the magnetic parameters as input in EPR spectral simulations by the EasySpin software. This procedure accounts for Lorentzian and/or Gaussian profiles allowing accurate comparison between simulated and experimental line widths. It is a direct method, compared to using the standard expressions for the coefficients *a*, *b*, and *c* of Eq. (3), see Ref. 12 and references therein.

2.1. Determination of methyl radical tunneling frequency

The effect of motional averaging of the EPR parameters anisotropy of methyl radical isolated in matrices of spherically symmetrical particles is considered in this work. The perpendicular rotation of methyl in these matrices is not hindered compared to matrices of linear molecules where strong hindrance is the case [20].

For CH₃ isolated in solid Ar, the approximate curve obtained in a least-squares fit of the experimental data is plot-

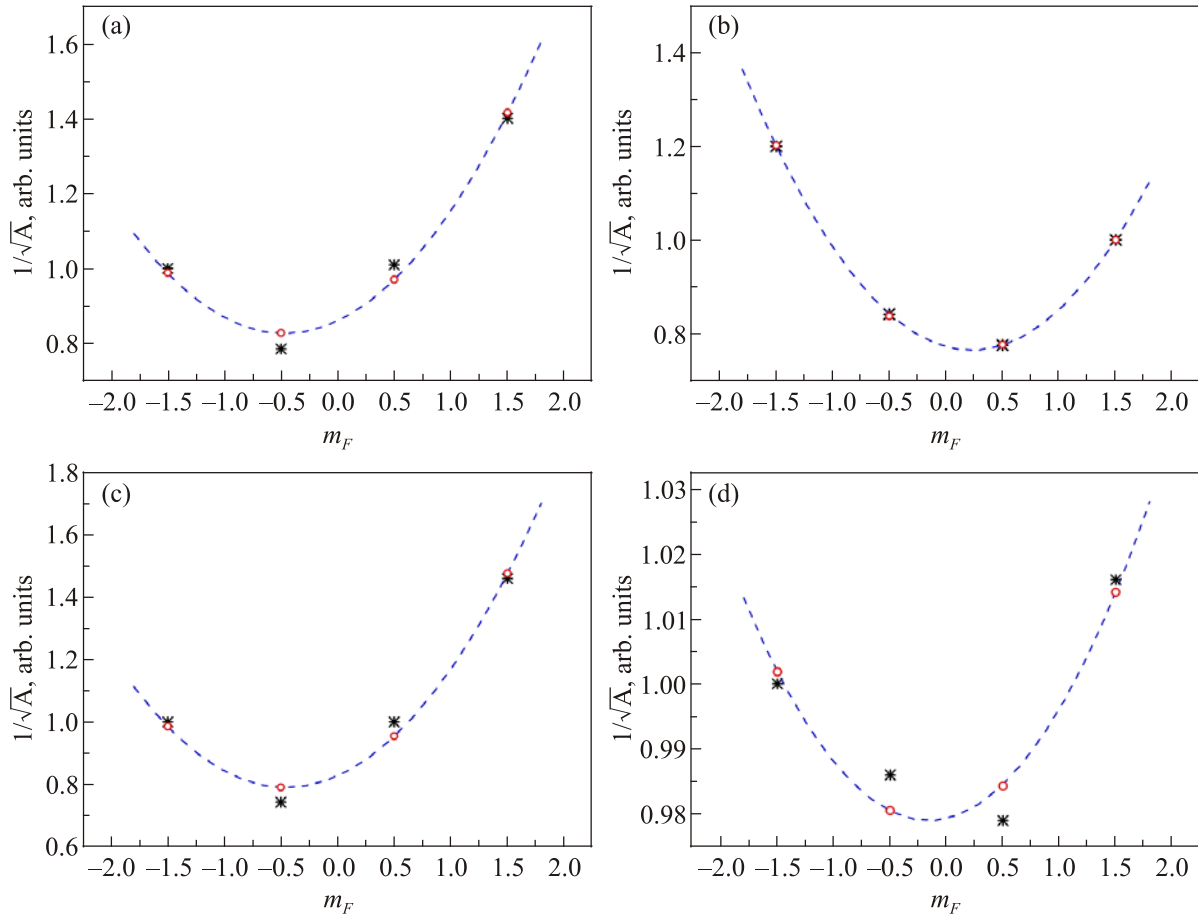


Fig. 1. (Color online) EasySpin simulations of the EPR spectra for matrix isolated CH_3 at 4.2 K in solid gases: in Ar (a), Kr (b), Ne (c), and para- H_2 (d). The reciprocal square root amplitudes of the hf components are plotted against the projection m_F of the three coupled-proton spin representation \mathbf{F} . The blue dashed line calculated using Eq. (3) fits the experimental data presented in black asterisks. The experimental data were taken from our earlier study [12]. The EasySpin simulation results indicated by red open circles are obtained with EPR parameters listed in the text.

ted in Fig. 1(a). To obtain the correlation time of the rotation, the simulation of the EPR spectrum with the EasySpin software [21] was performed in the fast-motion regime. The physical parameters of solid Ar and solid N_2 are close as anticipated by the full mutual solubility of the two components. Therefore, matrix shifts of the EPR parameters of methyl radicals trapped in Ar and N_2 solids are expected to be close. Referring to the hf couplings, they are, indeed, nearly equal: $-2.313(5)$ mT for CH_3 in Ar compared to $-2.317(5)$ mT for CH_3 in N_2 matrix [13]. The isotropic g -factor, however, shows a noticeable difference, $2.002322(56)$ and $2.00250(12)$ for CH_3 in Ar and N_2 solids, respectively. The g -factor matrix shift of methyl is due to admixture of the unpaired electron p -orbital of the radical with the frontier orbitals of the neighboring matrix particles. This effect is similar to the matrix isolated atomic hydrogen, whose g -factor matrix shift is obtained by admixture of its electron wave function with the p -orbitals of the nearest matrix particles after the required orthogonalization [22].

The principal quantum numbers of the orbitals of the outer (valence) Ar electrons are larger compared to the N_2 molecule and would lead to an increased g -factor shift. To verify this possibility, we performed test simulations keeping the \mathbf{A} -tensor anisotropy, $\Delta A = A_{\parallel} - A_{\perp}$, equal to that of CH_3 in solid N_2 , $\Delta A = 0.098$ mT, and changing simultaneously the \mathbf{g} -tensor anisotropy, $\Delta g = g_{\parallel} - g_{\perp}$, the individual line width, ΔH , and the τ_{corr} to obtain the best possible curve fitting. The isotropic parts of the \mathbf{A} - and \mathbf{g} -tensors were set equal to those of CH_3 in solid Ar: $A_{\text{iso}} = -2.313$ mT, $g_{\text{iso}} = 2.002322$. The individual line width was isotropic and the lineshape was Lorentzian. The best fit was obtained with $\Delta g = -1.73 \cdot 10^{-4}$, $\Delta H = 0.0086$ mT, $\tau_{\text{corr}} = 24$ ns. In Fig. 1(a), the results of the simulations fit well to the approximate curve. The peak-to-peak widths of the simulated hf components are $0.0248, 0.0163, 0.0141, 0.0172$ mT counting from low to high fields and match well with experimental widths [18] $0.0229, 0.0183, 0.0136, 0.0204$ mT.

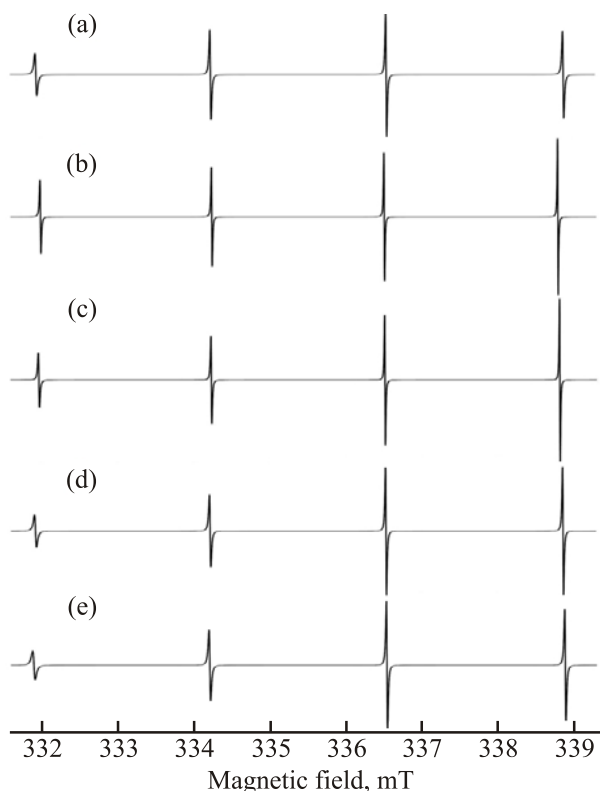


Fig. 2. EPR lineshape of CH₃ in solid Ar simulated using different values of the \mathbf{g} - and \mathbf{A} -tensor anisotropies. The microwave resonance frequency was $f_{\text{res}} = 9.4003$ GHz. The isotropic components of the tensors were set equal to those obtained experimentally: $g_{\text{iso}} = 2.002322$, $A_{\text{iso}} = -2.313$ mT. (a) $\Delta A \equiv A_{\parallel} - A_{\perp} = 0.098$ mT, equal to the value measured for CH₃ in solid N₂, $\Delta g \equiv g_{\parallel} - g_{\perp} = -1.73 \cdot 10^{-4}$, $\tau_{\text{corr}} = 24$ ns; (b)–(e) $\Delta g = -3.7 \cdot 10^{-4}$, equal to the value measured for CH₃ in solid N₂, and $\tau_{\text{corr}} = 20$ ns for all four simulations, whereas the \mathbf{A} -tensor anisotropy ΔA increases gradually as 0.3, 0.5, 1.0, 1.2 mT, respectively. Figure 1 evidences that the simulation (a) is very close to the experimentally measured amplitude ratios of the hf components of the spectrum recorded in the CH₃–Ar experiments.

To make a complete consideration, we tried another approach by fixing $\Delta g = -3.7 \cdot 10^{-4}$ equal to that of the \mathbf{g} -tensor anisotropy for CH₃ in solid N₂ [13] and changing the \mathbf{A} -tensor anisotropy. Figure 2 summarizes the EasySpin obtained simulations.

The upper spectrum is simulated using the EPR parameters listed above and fits well with the CH₃/Ar experimental data shown in Fig. 1(a). The next four simulated spectra show changes in the EPR lineshape with fixed Δg and gradual increase of ΔA . The simulations begin to resemble (however, poorly) the experimental results when a large value of the hf-tensor anisotropy, ΔA , is involved, not meeting the physics of the system. Indeed, the radical reorientation about the in-plane axes is considered as a combination of very fast small-angle librations with the frequency of the order of 10^{12} Hz and much slower full rotation with frequencies less than 10^9 Hz [20,24,25]. The aniso-

tropies Δg and ΔA , used in the spectral simulations, result from the rigid radical parameters, partially averaged by radical librations. Previously, the averaged anisotropies were shown to gradually decrease with decreasing eccentricity of the matrix molecules in the order, CO₂, N₂O, CO, N₂ [20]. Accordingly, ΔA for Ar matrix should be equal or somewhat smaller than N₂ matrix.

The case of Kr matrix is of particular interest. Indeed, the amplitude sequence of the EPR spectrum of CH₃ in solid Kr matrix is a mirror image of the CH₃ spectrum in practically all the other solid gas matrices, Ne, Ar, N₂, CO, N₂O, CO₂ [13,18,19]. This “mirror” effect originates from the opposite sign of \mathbf{g} -tensor anisotropy in Kr compared to Ar matrix [13,18], modifying the linear, cross relaxation term of Eq. (3). Another feature of the CH₃–Kr system is the largest matrix shift of the \mathbf{g} -tensor compared to CH₃ in other matrices [13], including solid gases, zeolites, vycor glass, beryl, methane hydrate, and feldspar. On the contrary, the CH₃–Kr hf coupling does not seem to demonstrate such striking matrix shift characteristics: the hf coupling anisotropy has the same sign as the CH₃–Ar system [13] and the hf coupling matrix shift is of moderate value [20]. The EPR transitions recorded in the CH₃–Kr experiments are somewhat broader [19] compared to those of the CH₃–Ar system. The extra broadening is due to that natural Kr contains 11.5 % of the magnetically active ⁸³Kr isotope that contributes to the superhyperfine broadening admixing in addition Gaussian profile to the EPR lineshape. On the basis of the hf component amplitude ratio [12] and the experimental line widths [19], an excellent EasySpin simulation is presented in Fig. 1(b). The line widths of the simulated spectrum, 0.0275, 0.0234, 0.0247, 0.0313 mT, counting from the low- to the high-field component, match extremely well with the experimental data [19]: 0.0301, 0.0218, 0.0241, 0.0334 mT. The EPR parameters used in the simulations for CH₃ in Ar, Kr, Ne, and para-H₂ are listed in Table 1. The isotropic \mathbf{A} - and \mathbf{g} -tensor components were set equal to those of CH₃ in solid gases from the previous study [13]. It was found that both the hf anisotropy, $\Delta A = A_{\parallel} - A_{\perp}$, and the \mathbf{g} -tensor anisotropy, $\Delta g = g_{\parallel} - g_{\perp}$, should be modified for best agreement of the simulations with the experiment.

As a result, the following values were obtained: $\Delta A = 0.138$ mT, $\Delta g = 1.13 \cdot 10^{-4}$, $\tau_{\text{corr}} = 17$ ns. The opposite sign of Δg compared to CH₃ in Ar stems from the greater matrix shift of the g_{\perp} component compared to the g_{\parallel} component reported earlier [13]. Comparing g_{iso} in the two noble gas matrices, it is concluded that Kr matrix affects the g -factor far more efficiently than Ar matrix. It is also worth to pay attention at the hyperfine tensor anisotropy yielded by the simulation. The value 0.138 mT lies between the anisotropies for CH₃ in N₂O and CO₂ matrices, being among the largest hf anisotropies for matrix isolated CH₃ in solid gases. The radical libration angles in the substitutional position of the regular solid Kr lattice are expected to be larger

Table 1. EPR parameters for CH₃ in solid gases used in the spectral simulations in Fig. 1. Isotropic hf coupling and **g**-tensor parameters are taken from Ref. 13. Notice the trend of decreasing rotational correlation time with increasing atomic radius of the host

Matrix	A_{iso} , mT	g_{iso}	ΔA , mT	Δg	ΔH , mT	τ_{corr} , ns
Ne	-2.333	2.002526	0.108	$-1.844 \cdot 10^{-4}$	0.0084(L)	28.5
Ar	-2.313	2.002322	0.098	$-1.73 \cdot 10^{-4}$	0.0086(L)	24
Kr	-2.300	2.001655	0.138	$1.13 \cdot 10^{-4}$	0.0045(L) 0.0156(G)	17
H ₂	-2.324	2.002516	0.1	$-0.6 \cdot 10^{-4}$	0.0045(L) 0.0196(G)	2.3

than in Ar and N₂ matrices because of the larger lattice constant of 6.13 Å in Kr, compared to 5.31 and 5.65 Å in Ar and N₂, respectively. Large-angle librations should, however, tend to decrease the hf anisotropy [20]. An explanation for this inconsistency could be the local rearrangement of the strained crystal lattice of quench-condensed Kr. The rearrangement of the cubic lattice to axially symmetric hexagonal affects the axial anisotropy of the EPR parameters. This process was suggested previously when considering axially symmetrical EPR of H-atoms trapped in quench-condensed Kr [26] and saturation peculiarities of CH₃ radicals in the same matrix [3].

Figure 1(c) shows the EPR lineshape simulation data of CH₃ trapped in solid Ne. The best lineshape fit was obtained with **g**- and hf **A**-tensor anisotropies close to the ones used in the Ar matrix simulation as shown in Fig. 1(a) and Table 1.

As a result, the correlation time $\tau_{\text{corr}} = 28.5$ ns is somewhat greater compared to Ar matrix. Solid Ne is a tighter matrix compared to the solid Ar as seen from the lattice parameters of 4.46 Å for Ne and 5.31 Å for Ar. As discussed above, a tighter matrix enables smaller radical libration angles, and less averaged anisotropies, yielding larger ΔA . The difference between the CH₃ radical hf **A**-tensor anisotropies in Ne and Ar would be more pronounced if it were not for the semi-quantum nature of solid Ne, characterized by fairly large zero-point displacement amplitude of the Ne matrix atoms.

A very small difference in the relative amplitudes of the CH₃ hf components was recorded for methyl radical trapped in solid para-H₂ [12]. In this case, even a small error in experimental amplitudes may result in rather large uncertainty in $1/\sqrt{A}$ as a function of the projection of the total nuclear spin. This is evident from Fig. 1(d) where the experimental points deviate more from the theoretical fitting curve compared to the noble gas curves in Figs. 1(a)–(c). The deviation taken in the percentage of the overall spread of the hf-line amplitudes is addressed here.

The EPR transitions recorded in the H₂–CH₃ experiment [12] were rather broad, with a peak-to-peak width of the third, $m_F = -1/2$, component 0.022 mT compared to approximately 0.01 mT expected for radicals isolated in magnetically silent matrices. Indeed, the width of the third

EPR hf component in solid Ar that has not magnetic isotopes is 0.014 mT. The small, extra broadening in para-H₂ is probably due to admixture of a small amount of ortho-H₂ molecules generated during the para-hydrogen radiofrequency discharge before sample condensation. The profiles of the simulated transitions were obtained as mixtures of Gaussian and Lorentzian components, applying 0.0045 mT Lorentzian width taken from the CH₃–Kr experiment. On the basis of this value, the experimental width of the Gaussian contribution to the lineshape was calculated as 0.0196 mT. The closeness between the amplitudes of the hf components for CH₃ in the para-H₂ lineshape made it difficult to select spectral parameters for best fitting. On the basis of results for the noble gas matrices, the estimated hf tensor anisotropy, ΔA , were of the order of 0.1 mT compared to 0.098 mT in Ar, 0.138 mT in Kr, and 0.108 mT in Ne.

As it was verified in the present study, the hf tensor anisotropy ΔA was not that sensitive to the matrix particles surrounding the radical species as was the **g**-tensor anisotropy. The nearest coordination distance of methyl to the matrix particles in solid H₂ and Ar was nearly the same: 3.76 Å. The hf anisotropy ΔA in solid H₂ is expected to be somewhat smaller than in Ar due to the quantum nature of solid hydrogen while on the contrary, the axial hcp (hexagonal close packed) crystal structure of H₂ favors increased ΔA .

The best fit, Fig. 1(d), was obtained with $\Delta g = -0.6 \cdot 10^{-4}$ and $\tau_{\text{corr}} = 2.3$ ns. The **g**-tensor anisotropy turned out to be the smallest among the matrices analyzed. This is because of more efficient averaging of the anisotropy by the significantly increased libration motion of the radical in the H₂ quantum crystal. The correlation time is far too shorter than for other matrices, since the trapped radical is much freer to rotate.

2.2. Motional averaging mechanisms of EPR anisotropy

Methyl radical reorientational motions about the C₃- and C₂-symmetry axes average partially the spin-Hamiltonian anisotropy depending mostly on the strength of the matrix-impurity Pauli repulsion [12]. The residual anisotropy may be observed in different amplitudes and widths of any of the hyperfine components, symmetric with respect to the base line, or as anisotropic splitting. The former type of the

anisotropy is common of CH₃ in molecular hydrogen H₂ and solid noble gases Ne, Ar, Kr [12,27], while the later was observed in solid gases consisting of the linear CO, N₂O, CO₂ molecules [13,14,20]. The rotational averaging is effective even at liquid helium temperatures due exclusively to tunneling. The present study is aimed at correlating tunneling rates to barriers of rotation for CH₃ in van der Waals solids, applying theoretical approaches describing the experimentally observed residual EPR anisotropy of trapped radicals.

Lack of direct experimental evidence of anisotropy even at liquid He temperatures is the case for the alpha-protons of free methyl, as only the high resolution 1:1:1:1 ground rotational EPR quartet is visible [11]. Pure quantum mechanical inertia rotation treatment required that methyl rotor stops at this temperature with only the above-mentioned spin-rotation state possible [11]. Therefore, all changes of the temperature-dependent hf line splitting were considered to be due to dynamics. Theoretical values of static magnetic parameters of methyl in vacuum coming from first principle quantum chemistry computations can be of importance for this purpose [13]. A great help for the disentanglement of the parameters was offered by the simulation of the high-temperature limit spectra that do not exhibit complications due to motional quantum effects.

The effect of molecular reorientation on the EPR lineshape is commonly involved in quantitative methods of molecular mobility data extraction. In low viscosity liquids, angular velocities of time scales less than 10⁻¹⁰ s are required to fully average the magnetic parameters of the probe, e.g., the nitroxide. Libration motion is also efficient averaging mechanism at the EPR time scale. The term libration is commonly used for harmonic angular oscillations of molecules in crystals with frequencies of 10¹¹ to 10¹² s⁻¹ and amplitudes of approximately 2–3 deg. A similar type of motion in glasses has been evidenced by high-frequency EPR, magnetization transfer, and spin-echo experiments [23,25]. However, low-temperature torsional oscillations greater than 8 deg were detected in the present work for tunneling methyl isolated in solid CO₂, *vide infra*. This motion seems to correlate with unusually wide “hopping precession” angles of the linear CO₂ molecules discovered recently by Krainyukova and Kuchta [5] in frozen samples of pure CO₂.

Due to libration, the anisotropies of methyl spectra were partially averaged as shown earlier [20], gradually decreasing with decreasing eccentricity of the matrix molecules in the order: CO₂, N₂O, CO, N₂. Our analysis showed that the greatest uncertainty in obtaining rotational correlation times was associated with the approximation of the obtained polynomial coefficients in Eq. (3). It turned out that the relative errors were least for *a*, while *b* and *c* showed somewhat larger error than *a*. As a result, the EasySpin simulations yielded cautious estimate of τ_{corr} error of about 4 ns relative to the shifts in *b* and *c* coefficients.

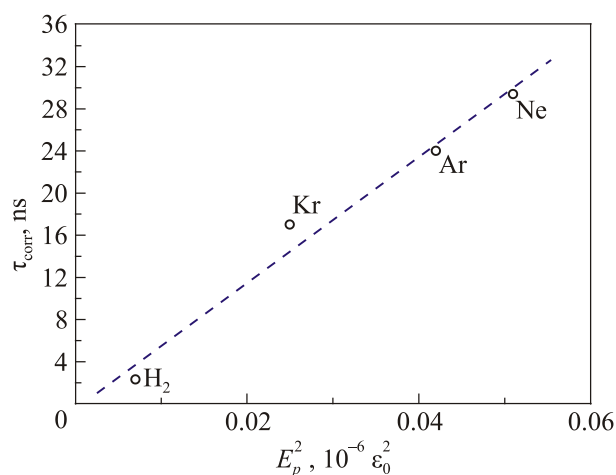


Fig. 3. Correlation time of the perpendicular rotation of CH₃ radical in various matrices plotted against the squared Pauli repulsion energy E_p^2 , where $\epsilon_0 = 27.212$ eV, is the Hartree atomic unit of energy.

Figure 3 shows the rotational correlation time plotted against the squared Pauli repulsion energy E_p^2 . The figure establishes a linear correlation between rotation hindering and repulsion of the trapped CH₃ radical by the matrix particles. It is suggested in the present study, that the averaged spectrum anisotropy is not only a function of τ_{corr} and the radical–matrix interaction but depends also on the lattice symmetry of the matrix. The influence of the matrix symmetry on the anisotropy of the radical EPR parameters is readily seen from the experimental and theoretical studies of trapped H atoms.

Free atomic hydrogen is characterized by spherically symmetrical electron wave function and isotropic hf constants. When trapped in solids, H atom reveals wave function of reduced symmetry adapting to the electrostatic potential of the cage formed by the matrix first couple of coordination spheres. As a consequence, excluding cubic lattice, the hf interaction develops appreciable anisotropy [28–31]. The excellent linear fit in Figure 3 may be accidental. Further experimental work with Kr matrices with unstrained crystal lattice, condensed, e.g., at temperatures well above 4.2 K, is required for the verification of the linearity.

3. Rotary tunneling vs. hindering barrier of methyl radical

Even strongly hindered methyl groups can perform rotary motion at very low temperature in the sense that quantum mechanics allows penetration of the torsional barrier. A periodic C₃ potential with periodic boundary conditions will be further considered hindering coherent leakage of methyl to the adjacent minima with “distance” 120 deg. The rate of this rotary motion of methyl can be faster than the proton hfi (hyperfine interaction) measured in MHz. The situation can be the reverse for systems with high bar-

riers. The deuteron rotor, e.g., is normally much slower, *vide infra*, due to the “dramatic” increase of the inertia by factor two.

The point here is that one has to use a quantum description of the motion in order to reproduce the experimental effects on the EPR lineshape, at least for the lowest temperatures close to 5 K. We can use, e.g., approximate harmonic oscillator states localized at the minima of the potential energy wells for the description of this motion, see Appendix. Certainly, Hermite polynomials, or any other simple choice like Gaussians [32], cannot be accurate eigenfunctions of a Hamiltonian with an actually periodic potential but they can be used as (zeroth order) basis functions for the approximate solution of the problem.

Briefly, the approximate localized functions of the smallest C_3 group are giving initially an equal number of degenerate basis-functions $\Psi_v^{(k)}(\varphi) \equiv \Psi_v^{(k)}(\varphi - \vartheta_k)$ with location $k = 0, \pm 1$, seen in the correlation diagram, Fig. 4. The angles $\vartheta_k = kp$ are given in terms of the period of the potential energy $p = 2\pi/3$. The index $v = 0, 1, 2, \dots$ of the above functions stands for the vibration level.

The eigenvalues of these functions are given by

$$E_v = 2\beta B(v + \frac{1}{2}), \quad \beta = \frac{3}{2}\sqrt{\frac{V_3}{B}}, \quad (4)$$

where B is the rotational constant and the variable $\beta = (3/2)\sqrt{V_3/B}$ is expressed in terms of the just mentioned constant B and the barrier V_3 , as seen in Appen-

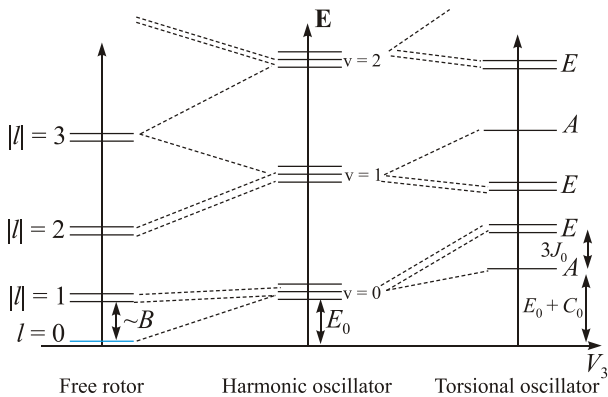


Fig. 4. Correlation diagram showing roughly the connection between the three different types of rotary/torsional motions. Notice that the three vertical axes cannot be put in a universal scale since the transition frequencies is a multivariate quantity. The ground rotation level has been lifted by the zero-point vibration energy $E_0 = 3(BV_3)^{1/2}/2$. The first order correction of the torsional level amounts to C_0 , see Appendix. The tunneling frequency of the ground vibrational level is designated by $3J_0$. Going from the left to the right, the second diagram corresponds approximately to the librating radical, while the third diagram to the right is for the radical performing rotation around the C_3 axis by tunneling through the barrier with frequency $3J_0$. In the end of this section, the description of this motion physics is provided.

dix A. The 3-fold degeneracy of the above-localized vibrator eigenfunctions can be lifted by a periodic potential if the barrier between adjacent wells is not infinitely high. The problem can be solved by both degenerate perturbation or by the variational method [33]. The variational principle is formally more appropriate because the basis functions of the localized torsional oscillators cannot be orthogonal as they overlap. As it will be shown later, the overlap, however, is small for all practical purposes.

E.g., the overlap of the lowest (ground) torsional level with quantum number $v = 0$ is given by

$$S_0 \equiv \langle \Psi_0^{(k)}(\varphi) | \Psi_0^{(k\pm 1)}(\varphi) \rangle = \exp\left\{-\frac{\pi^2}{6}\sqrt{\frac{V_3}{B}}\right\}. \quad (5)$$

This equation is plotted in Fig. 5 and indicates that the overlap is not really significant in the present case.

In spite of that, the solution of the tunneling frequency vs. potential problem obtained by this way will not be as accurate as a numerical solution model starting from free rotor in presence of a periodic potential. In practice, it was not easy to make the solutions of the perturbative kind accurate enough, see Fig. 6(a). However, the motivation of seeking such a solution, in addition to relatively easily obtainable numerical ones, is rather the transparency and the usefulness in the physical interpretation of several effects. Symmetry considerations play a very important role here.

Further, one should remember that the analytical expressions in the present work are approximate. The assumptions are: i) consideration of parabolic zero order potential; ii) neglect of the mixing with higher vibrational levels.

The parabolic potential was obtained by Taylor–Maclaurin series expansion of the periodic C_3 potential

$$V(\varphi) = \frac{V_3}{2} [1 - \cos 3\varphi]. \quad (6)$$

Finally, the mechanism of the tunneling rotation of the radical can be described as a quantum effect by the time-

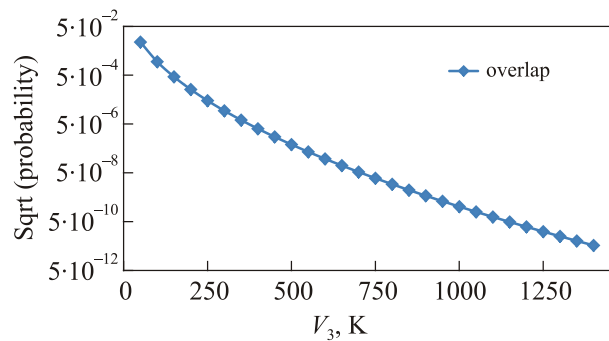


Fig. 5. The overlap S_0 of the adjacent vibrator eigenfunctions for the ground torsional level of methyl according to Eq. (5). Notice that the value of this integral is very small already for potential barriers $V_3 > 100$ K and becomes virtually insignificant after 250 K. Those potentials are in compatible order of magnitude for methyl rotor systems studied in the present work ($1.000 \text{ K} = 2.0837 \cdot 10^4 \text{ MHz}$).

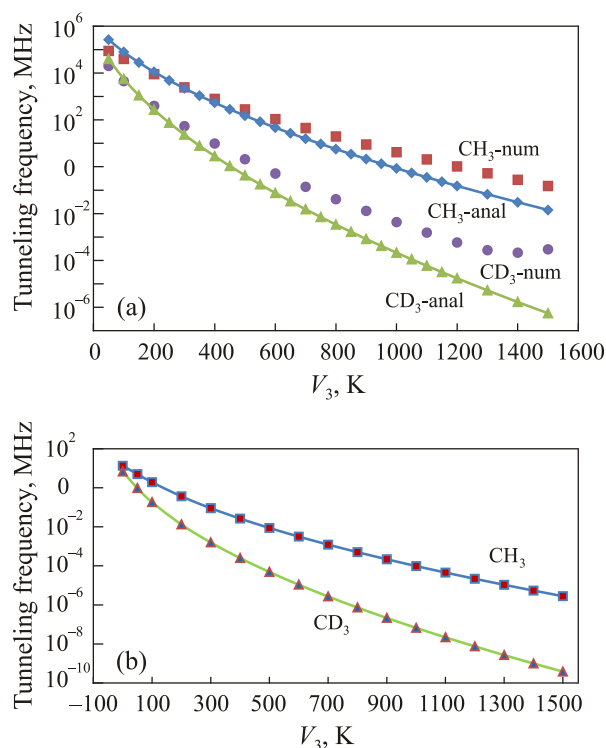


Fig. 6. (a) CH₃ and CD₃ tunneling frequencies about the C_3 axis for different values of the barrier V_3 keeping the value of the kinetic constants $B = 6.752$ and 3.376 K for protonated and deuteriated methyl, respectively ($1 \text{ K} = 20.837 \text{ GHz}$). The upper limit of the tunneling frequency for $V_3 = 0$ is formally equal to the rotational constant B . (b) Plot of the numerically obtained tunneling frequency vs. potential barrier of methyl and deuteriated methyl about any in-plane C_2 axes of the radical. The computational method was parallel to the approach for the C_3 case. The details of the method are described in Appendix C.

dependent Schrödinger equation. The diagonalizing transformation of the localized vibrator eigenfunctions leading to the torsional oscillator eigenfunctions can be inverted and the former set can also be used in the time dependence of the system. In that case, if the initial state of the system is in one of the potential wells, it will be found in any of the two adjacent wells at a time equal to the inverse energy difference of the $E-A$ states, signifying the quantum tunneling of the system over the potential barrier.

3.1. Computation of the tunneling frequency

One of the aims of this work is to derive analytical expressions for the tunneling frequency $3J_0$ vs. the potential barrier V_3 . Hence, a combination of the perturbation and the variational methods were tested. The value of the overlap integral $S_v = \langle \Psi_v^{(k)} | \Psi_v^{(k\pm 1)} \rangle$ of any two adjacent localized torsional oscillator eigenfunctions was originally omitted in the computation of the perturbation treatment because it is very small for the case here $V_3 \gg B$. This is at least veri-

fied for the lowest vibrational levels as shown in Fig. 5, which is a plot of the overlap vs. barrier shown in Eq. (5).

The inclusion of the overlap in a more accurate analytical expression for the torsional splitting of the ground level according to the variational theory has also been investigated. When this effect was included it did not help practically, because on the contrary, for low-potential barrier where the overlap is important the analytical expression obtained by perturbation gave better agreement with the numerical result. For high-potential barrier where the disagreement worsens for the perturbation method, the overlap is very small, and the variation method yielded the identical result as the perturbation.

Also, ENDOR has been used to determine tunneling frequency. The theoretical treatment of the shift of ENDOR transitions due to tunneling is usually obtained by using the second order perturbation theory of an effective spin-Hamiltonian [34,35]. The potential barrier is then deduced by numerical simulations involving a series of barriers and computing the energy difference between the two lowest levels [34]. Hence, we tried to obtain the most natural analytic expression of the tunneling frequency vs. the potential barrier described further in the text.

Figure 6 shows the tunneling frequency of the parallel rotation of both protonated and deuteriated methyl radicals vs. potential barrier. The numerical method is based on diagonalizing the pure rotational Hamiltonian including a hindering periodic C_3 potential in the basis set of a two-dimensional free rotor. Similarly, the analysis of the tunneling rotation about the in-plane axes is based on a C_2 symmetry potential with periodic boundary conditions.

The analytical computation of the C_3 case is based on the degenerate perturbation treatment of localized torsional Hermite polynomial oscillator eigenfunctions. Both the barriers of the protonated and the deuteriated methyl radicals were computed and compared. One good reason for studying also the deuteriated CD₃ values is that often the EPR spectra of deuteriated methyl are misinterpreted in literature. Look for the experimental EPR data along with the corresponding accurate theoretical predictions shown in Ref. 11.

In Fig. 6, the method used in the computations, either numerical, or deriving analytic expressions using the perturbation theory on assumed localized oscillators is indicated. The Hermite polynomials are eigenfunctions of these oscillators inside each potential well of the two- or three-fold symmetry axis of rotation. The diagonalization of the following matrix for the rotational Hamiltonian in presence of the C_3 potential $V(\varphi)$ in Eq. (6) will result in the corrected, albeit approximate, energies for the torsional oscillator

$$\mathbf{M}_v = \begin{pmatrix} & \Psi_v^{(-1)} & \Psi_v^{(0)} & \Psi_v^{(+1)} \\ \Psi_v^{(-1)} & D_v & J_v & J_v \\ \Psi_v^{(0)} & J_v & D_v & J_v \\ \Psi_v^{(+1)} & J_v & J_v & D_v \end{pmatrix}. \quad (7)$$

The diagonal matrix elements D_v in the isolated oscillator basis set contain the regular quantum vibrator energy E_v and the first order correction C_v due to the potential $V(\varphi)$, see Appendix. The off-diagonals matrix elements J_v between adjacent oscillators are also shown there. Notice that their nature, the number, and the presence even at the outer off-diagonals positions of matrix \mathbf{M}_v in Eq. (7), incorporate the physical meaning of periodic boundary conditions, necessary for the present case.

Diagonalizing the above matrix, the eigenvalues $E_A = D_v + 2J_v$ and $E_{E\pm} = D_v - J_v$ of the system, corresponding to the totally symmetric A , and the doubly degenerate E -symmetric torsional level, respectively, were obtained. The second order tunneling frequency $f_{v,\text{tun}}$ amounts to the difference

$$f_v = E_{E\pm}, -E_A = D_v - J_v, -(D_v + 2J_v) = -3J_v \quad (8)$$

which is shown in the next equation explicitly in terms of the barrier V_3 and the rotational frequency B

$$f_{0,\text{tun}}^{(2)} = -3J_0^{(2)} = \frac{3V_3}{2} \exp\left[-\left(\frac{\pi^2}{6}\sqrt{\frac{V_3}{B}}\right)\right] \times \left\{1 - \frac{3\pi^2}{2} - \frac{9}{2}\sqrt{\frac{B}{V_3}} + \exp\left[-\left(\frac{3}{2}\sqrt{\frac{B}{V_3}}\right)\right]\right\}. \quad (9)$$

This expression for the tunneling splitting of the ground level is usually designated by $3J_0$ [30]. In the present work, the tunneling frequency is obtained by including the contribution of the full second-order effects concerning the periodic potential, as shown in Appendix.

There are several treatments in the literature with varying terminology where the symbol J_0 , or similar, has been used identically as the $\langle \psi_v^{(k)}(\varphi) | V(\varphi) | \psi_v^{(k\pm 1)}(\varphi) \rangle$ matrix element and/or as an empirical constant for the tunneling frequency in a pure spin-Hamiltonian. To distinguish with the present full second-order degenerate-perturbation treatment, we will use the symbol J_0 for the off-diagonal matrix element $\langle \psi_v^{(k)}(\varphi) | H'(\varphi) | \psi_v^{(k\pm 1)}(\varphi) \rangle$ for the perturbation part of the rotational Hamiltonian $H_R = H_0 + H'$, seen in the Appendix, [36].

According to another interpretation, the tunneling frequency is the energy difference of the two lowest levels of the above-hindered rotation Hamiltonian. The relevant numerical computations were performed in the more convenient basis set of the normalized, Bloch type, exponentials $\{\exp(-in\varphi)/2\pi; n \in \mathbb{Z}^\pm, \varphi \in [-\pi, \pi]\}$. They were used to span the Hamiltonian matrix in the two-dimensional rotational space of a full cycle for a rotor influenced by the simplified hindering potential seen in Eq. (6). The matrix representation of this Hamiltonian was physically blocked by symmetry in three different sub-matrices, an A -symmetry block accompanied by an E_a and an E_b symmetry blocks. The computational details of the matrix elements and the

computations of the tunneling frequency vs. barrier V_3 are shown in Appendix B and visualized in Fig. 6.

This way of working corresponds to separating the three-dimensional (3D) quantum rotator considered by the Popov and coworkers [24] into either a C_3 or a C_2 methyl-axis rotation under different hindering conditions. They studied in detail how different orientations of the radical rotation axis with respect to a cubic matrix cage determine the strength and symmetry of the hindering barrier. In practice, matrix isolated methyls are embedded in well-defined host cavities restricting the direction of rotary motion not allowing free 3D motion. The restriction of the angular momentum projection with respect to a laboratory-defined frame reduces significantly the rotational degeneracy even in cases where the rotation appears practically free [17,20]. The numerical method of the present work can easily be extended to involve even more sophisticated potentials, exploiting the work of Popov and coworkers [24], provided that the matrix elements of the relevant potential can be computed in the given exponential basis set.

The explicit analytical expressions of the present work are not valid for very small $V_3 < 50$ K because of the method of approximation. However, for very low barriers of the order of 20–25 K and lower, it is expected that the “tunneling” frequency will be close to the rotational constant B as “free” rotation is approached and formal equality to B will be valid even at liquid He temperatures.

In spite of the qualitative agreement of the above expression in Eq. (9) with the numerical computation, the two series of values of the tunneling frequency follow each other rather well in the whole interval of the quotient V_3/B . The trend of the numerical computations for the two different rotors, proton, and deuteron, are also followed in the whole interval of the independent variable V_3/B , see Fig. 6.

However, the analytical values underestimate the numerical tunneling frequency more and more for larger values of the quotient V_3/B . One should expect the best agreement for large values of V_3 relative to B where the overlap is the least. In reality, this statement holds for the absolute values of the two different computational results, while progressively along with increasing V_3 , the analytical value of the tunneling frequency worsens in percent units.

A formally more appropriate method than perturbation should be the variational method, irrespective of the kind of the used trial functions Ψ . The reason is that the basis functions that were used for the perturbation treatment were not orthonormal, because the eigenfunctions of the well oscillators used are partially overlapping for the potential barriers of interest. According to the variational method, minimization of the integral quotient $\int \Psi^* H_R \Psi d\varphi / \int \Psi^* \Psi d\varphi$, should be performed. However, consideration of the missing overlap $\int \Psi^{(k)*} \Psi^{(k\pm 1)} d\varphi$, of the localized Hermite-polynomial basis used in the computations of the perturbation did not improve the result. At least, according to the variational method, only an upper estimate of the energy can be achieved.

As seen also in the plot of Fig. 5, the values of the overlap integral are negligible for the barriers of interest. A test of a more careful consideration according to the above lines did not improve the result, thus justifying the present investigation. It remains then to give an explanation and a suggestion for improving the analytical result.

4. Parallel and perpendicular methyl radical tunneling frequencies

The periodic C_2 and C_3 hindering potentials used in the computations of the present work is an approximation that simply indicates tunneling rotation about the in-plane axes or the higher symmetry axis of methyl radical, respectively. The obtained results on the tunneling-frequency vs. rotation-barrier are similar but the magnitude of the barrier and the periodicity of the potential determined the final details. An improved approach for more realistic potentials was presented by Popov, Kiljunen *et al.* [8,24], quantifying appropriate structural/geometrical parameters of the system, potentially useful for numerical simulations. Using the group theory, they incorporated the particular cubic cage geometry and the O_h symmetry of the host in combination to the intrinsic C_3 methyl symmetry into the final form of the hindering potential, where in addition radial conditions were involved.

Figure 7 and Table 2 show results based on the analytical C_2 treatment. The correlation times obtained from the EPR simulation of CH₃ in matrices of the spherical particles Ar, Kr, Ne and p -H₂, presented in Fig. 1(a)–(d), were used to derive the potential barriers. Figure 7 also shows an approximate exponential graphical fitting of the numerically obtained potential barriers from the tunnelling frequencies. Diagonalization of the hindered rotation Hamiltonian was used in both the above C_2 rotation case as well as for the following C_3 case.

Table 2. The obtained correlation times considered as invert tunneling frequencies of the CH₃ rotor isolated in four solid gases in the first section of this work along with numerically computed potential barriers V_3

System	τ_{corr} , ns	f_{tun} , MHz	V_3 , K
Linear host CO, N ₂ O, CO ₂ -CH ₃	710	1.4	1012
Ne-CH ₃	28.5	35.1	690.5
Ar-CH ₃	24	41.7	673.3
Kr-CH ₃	17	58.8	638.9
Spherical host para-H ₂ , Ne, Ar, Kr	~10	~100	585.8
p H ₂ -CH ₃	2.3	435	438.8

Figure 8 shows the computed barriers corresponding to observed tunneling frequencies obtained from the experimental spectra simulations for linear and spherical host molecules discussed in the present study and also in Refs. 2, 4, where estimations of possible C_3 symmetry barrier values are found for a comparison. The matter of the fact is that the frequency of 1.4 MHz is found for rotation about the

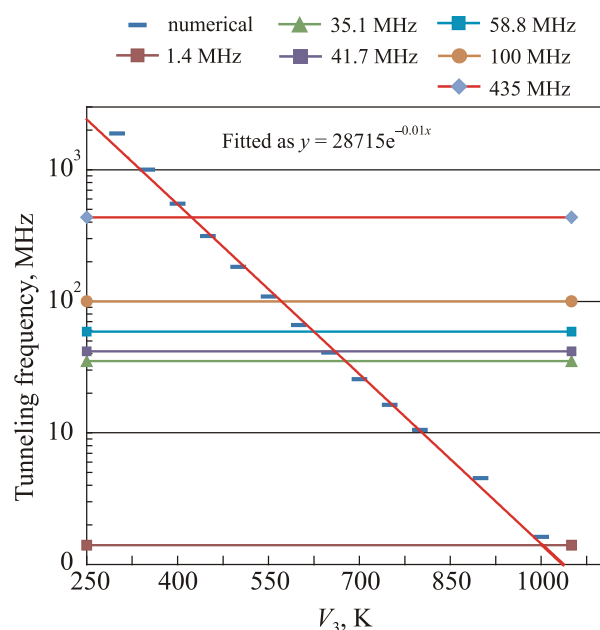


Fig. 7. (Color online) Computed tunneling frequency vs. potential in K for C_2 rotation (blue dash –), in the range of six different, experimentally determined, tunneling frequencies. The values in Table 2 were obtained by fitting the experimental tunneling frequencies the range $250 \text{ K} < V_3 < 850 \text{ K}$ to the exponential function $f_{\text{tun}} = 28715 \exp(-0.01V_2)$ MHz. The agreement with the numerically obtained values for C_2 symmetry tunneling with the straight line featuring the logarithm of the latter exponential relation was remarkable.

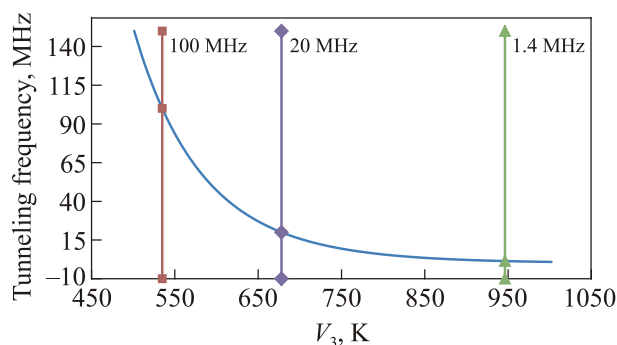


Fig. 8. Graphical representation of the numerically computed barriers vs. tunneling frequency for rotational frequency parameter of planar methyl $B = 6.752 \text{ K}$. Left for tunnel frequency $0.1 \text{ GHz} = 100 \text{ MHz}$ barrier $V_3 = 534.9 \text{ K}$, middle for frequency 20 MHz barrier $V_3 = 678 \text{ K}$, and right, for frequency 1.4 MHz barrier $V_3 = 946.2 \text{ K}$.

in-plane C_2 axes and concerns methyl radicals in matrices of linear molecules: CO, N₂O, CO₂. In this case, a barrier of 1012 K was obtained as shown in Table 2. However also a C_3 tunneling of this type of systems gives the same order of magnitude barriers, ca. 946.2 K, as obtained from the graphical representation of Fig. 8. On the other hand, tunneling frequencies ca. 0.1 GHz are obtained for matrices of

spherically symmetrical particles: para-H₂, Ne, Ar, Kr. Here, the corresponding barrier for C₃ tunneling is approximately 534.9 K as seen in the graphical representation of Fig. 8, which is in good agreement with 585.8 K for the C₂ tunneling shown in Table 2.

The EPR spectra of both CH₃ and CD₃ adsorbed on the silica gel surface at 77 K were studied by Gardner and Casey [37]. The dependence of the line width on the nuclear spin quantum number was interpreted in terms of the tumbling of the radicals on the surface and the values of the experimental correlation times/tumbling frequencies were determined as a function of the hyperfine **A**- and **g**-tensors anisotropy. Gardner and Casey obtained tumbling frequencies, 2.0·10⁷ and 1.3·10⁷ s⁻¹ for CH₃ and CD₃, respectively. Although rapid, these tumbling frequencies still indicate a considerable hindrance to methyl rotation by the silica gel surface, as free rotational frequencies are usually by three orders of magnitude (10³) faster. The hindering potential barriers determined by the presently developed barrier/tunneling relations indicate in particular barriers of ca. 678 K for the protonated and 326.8 K for the deuteriated methyl radical.

It seems that the eccentricity of the matrix molecules contributes to both the form and the height of the barrier and should be utilized in the determination of the potential barrier characteristics. It is certainly correlated to the libration motion or the hopping precession of linear molecules in the sense put forward by Krainyukova and Kuchta [5], which does not occur in case of matrices of spherically symmetrical particles. During the libration or hopping precession, a matrix molecule sweeps a cone which thus is not available to the methyl radicals. Evidently, the larger the molecule eccentricity, the larger is the cone volume, i.e., the barrier width and height. Although this picture is not directly suitable to apply in a mathematical model for the potential energy, it may be considered as a direction to follow in understanding the role of the eccentricity.

Namely, the occurrence of such a complicated EPR spectrum of the CH₃ radical in solid N₂O and CO₂ matrices, in contrast to solid rare gases and in N₂ and CO matrix isolation, depends on the relation between the structure of the hosted radical and the lattice molecules [4]. An appropriate quantity reflecting our qualitative considerations is the host molecule eccentricity ϵ taken simply as the ratio of the maximum of the internuclear distance d to the lattice parameter a . The results are summarized in Table 3 together with the relevant parameters supporting the above presumption. Indeed, no weak orthorhombic satellites were observed at temperatures above 8 K in CO and N₂ matrices [2,14,20] which have relatively small eccentricity, neither such spectra were reported for matrices of spherical symmetrical host particles. On the other hand, the matrices with larger eccentricity, such as N₂O and CO₂, show well discerned weak-line multiplet.

Table 3. Estimation of the molecule eccentricity for various cryocrystals at 20 K. The parameters d and a are available from Ref. 1

Matrix	Internuclear distance $d, \text{Å}$	Lattice parameter $a, \text{Å}$	Eccentricity $\epsilon = d/a$
N ₂	1.098	5.658	0.193
CO	1.128	5.652	0.200
N ₂ O	2.312	5.641	0.410
CO ₂	2.320	5.554	0.418

5. Conclusion

We first obtained rotation correlation times (tunneling frequencies) of the CH₃ radical in matrices of spherically symmetrical host particles held at liquid helium temperatures. The tunneling rates are correlated to the radical–matrix coupling leading to rotation hindering, mainly governed by the Pauli exclusion forces between trapped radical and matrix molecules.

Matrix shifts of spectrum anisotropies in trapped radicals testified that matrix effects are more important on Δg than on ΔA . Quench-condensed Kr crystallizes most probably into axially symmetric hcp local structure, surrounding the trapped CH₃ radical.

The theoretical treatment of this study explains how the fast orientational motion of methyl at low temperatures averages to different degrees the anisotropy of certain magnetic parameters due to rapid rotary tunneling about its C₃ and C₂ symmetry axes allowing estimation of the potential barriers to the rotation.

A clearly higher barrier of methyl rotation for the radical isolated in matrices of linear vs. spherical matrix molecules was obtained by evaluating the barrier of experimentally obtained tunneling frequencies. In particular, the linear CO, CO₂, N₂O molecular matrices seem to hinder tunneling methyl more efficiently than matrices of spherical molecular particles such as Ar, Kr, Ne and *p*-H₂. The barriers that the above linear molecular matrices oppose are slightly over 1000 K for both C₂ and C₃ rotational tunneling, which is almost double the barriers opposed to methyl tunneling by the above-mentioned spherical ones.

Appendix A. Torsional oscillator equations

The zero order eigenfunctions of the torsional oscillator for a three-fold periodic potential, with period $p = 2\pi/3$, and periodic boundary conditions, can be approximated by the following localized harmonic oscillator eigenfunctions:

$$\Psi_v^{(k)}(\varphi) = N_v H_v(x_k) e^{-x_k^2/2}. \quad (\text{A.1})$$

The Hermite polynomials H_v have the scaled angular coordinate argument x_k , given by

$$x_k = \sqrt{\beta(\varphi - \vartheta_k)} \quad (\text{A.2})$$

with a specification for the k th well position by the angle $\Theta_k = kp$ numbering the potential energy minima at the wells by $k = 0, \pm 1$, where $p = 2\pi/3$ is the period. The k -independent normalization factors N_ν of the above eigenfunctions are given in the following equation:

$$N_\nu = \left(\frac{\sqrt{\beta}}{2^\nu \sqrt{\pi \nu!}} \right)^{1/2}. \quad (\text{A.3})$$

The constant β is the square of the angle-scaling factor of the argument x_k given by

$$\beta = \frac{3}{2} \sqrt{\frac{V_3}{B}}, \quad (\text{A.4})$$

where V_3 is the potential barrier and

$$B = (h/2\pi)^2 / 2I \quad (\text{A.5})$$

is the rotation constant. This parameter represents the rotational frequency of planar methyl and has approximately the value 6.752 K for the protonated and half that value, 3.376 K, for deuteriated methyl radical species. The denominator of Eq. (A.5) gives the parallel component of the methyl rotor moment of inertia I , corresponding to rotation about the highest symmetry C_3 axis of a planar methyl.

The rotational constants according to Prager and Heidemann [38] are $B(\text{CH}_3) = B(\text{CH}_4) = 0.655 \text{ meV} = 7.601 \text{ K}$ ($1 \text{ eV} = 1.1605 \cdot 10^4 \text{ K}$), a value corresponding to the nonplanar $-\text{CH}_3$ fragment, that agrees with the one adopted in our previous work [11]. Popov *et al.* [24] and Kiljunen *et al.* [8] consider instead as rotational constant the double B value, equal to the inverse moment of inertia.

The above relations are based in the Taylor expansion of the potential $V(\varphi)$ (6) about its three minima. The resulting approximate harmonic potential $V'(\varphi) = 9V_3\varphi^2/4$ is seen in the following differential operator, used as the unperturbed part of the torsional Hamiltonian at each well:

$$H_0 = -B\partial^2 / \partial\varphi^2 + \frac{1}{2}(9V_3/2)\varphi^2. \quad (\text{A.6})$$

The following energies were obtained for the localized torsional levels:

$$E_\nu = 2\beta B(\nu + 1/2). \quad (\text{A.7})$$

Notice that this is a harmonic oscillator Hamiltonian that approximates the periodic potential energy by a parabola about each minimum. However, because the periodicity is not present in the approximate $V'(\varphi)$, an additional task is to imply it at a later stage.

The perturbation applied to the above zero order Hamiltonian was

$$H' = V(\varphi) - 9V_3\varphi^2/4. \quad (\text{A.8})$$

The potential energy $V(\varphi)$ is given in the above Eq. (6). The result obtained after the summation of the terms in Eqs. (A.6) and (A.8) is the identical total rotational Hamiltonian H_R :

$$H_R = -B\partial^2 / \partial\varphi^2 + V(\varphi) \quad (\text{A.9})$$

that comprises the full periodic potential.

Appendix B. Derivation of matrix elements

The following matrix elements were used in the treatment mentioned in the above Appendix A concerning the ground harmonic vibrational level. They are the diagonal (B.1) and the position overlap (B.2) of the square of the angular relocation variable φ .

The expression for the variance of the angle φ of the level ν for the localized vibrator given by

$$\langle \psi_\nu^{(k)}(\varphi) | \varphi^2 | \psi_\nu^{(k)}(\varphi) \rangle = \frac{(2\nu+1)\sqrt{B}}{3\sqrt{V_3}}. \quad (\text{B.1})$$

Next, the off-diagonal matrix elements of the square of the angular relocation variable φ is given

$$\begin{aligned} & \langle \psi_0^{(k)}(\varphi) | \varphi^2 | \psi_0^{(k\pm 1)}(\varphi) \rangle = \\ & = \frac{\sqrt{B}}{3\sqrt{V_3}} \exp\left(-\frac{\pi^2}{6} \sqrt{\frac{V_3}{B}}\right) \left[1 + \frac{\pi^2}{3} \sqrt{\frac{V_3}{B}} \right]. \end{aligned} \quad (\text{B.2})$$

The above two matrix elements were further computed for the full hindering potential $V(\varphi)$:

$$C_0 = \langle \psi_0^{(k)}(\varphi) | V(\varphi) | \psi_0^{(k)}(\varphi) \rangle = \frac{V_3}{2} \left[1 - \exp\left(-\frac{3}{2} \sqrt{\frac{B}{V_3}}\right) \right]. \quad (\text{B.3})$$

This term is the first-order potential energy correction to the energy E_0 in Eq. (A.7) of the ground vibrator eigenfunction, obtained as a particular case of the following general ν level vibrator correction:

$$\begin{aligned} C_\nu & = \langle \psi_\nu^{(k)}(\varphi) | V(\varphi) | \psi_\nu^{(k)}(\varphi) \rangle = \\ & = \frac{V_3}{2} \left[1 - \exp\left(-\frac{3}{2} \sqrt{\frac{B}{V_3}}\right) \sum_{l=0}^{\nu} \frac{(-1)^l}{l!} \left(\frac{3}{\sqrt{2\beta}}\right)^{2l} \binom{\nu}{l} \right]. \end{aligned} \quad (\text{B.4})$$

On the other hand, except for the ground level, the general expressions of the higher level off-diagonal matrix elements of the potential are particularly difficult to obtain. For the ground level we have

$$\begin{aligned} J_0 & = \langle \psi_0^{(k)}(\varphi) | V(\varphi) | \psi_0^{(k\pm 1)}(\varphi) \rangle = \\ & = \frac{V_3}{2} \exp\left(-\frac{\pi^2}{6} \sqrt{\frac{V_3}{B}}\right) \left[1 + \exp\left(-\frac{3}{2} \sqrt{\frac{B}{V_3}}\right) \right]. \end{aligned} \quad (\text{B.5})$$

The diagonal matrix elements for a general vibrational level ν were first computed by paper and pencil and were reduced for the ground level by putting $\nu = 0$. The matrix elements were then verified by comparing to expressions obtained with ‘‘mathematica’’.

Appendix C. Numerical treatment

The matrix elements of the quantum rotation Hamiltonian under the influence of a hindering potential, $H_R = -B\partial^2 / \partial\varphi^2 + V(\varphi)$, in the Bloch type, imaginary exponential basis set $\{N \exp(-in\varphi) : n \in \mathbb{Z}^\pm, \varphi \in [-\pi, \pi]\}$, are given by combining the orthogonality relation

$$\int_{-\pi}^{\pi} \left(e^{-im\varphi} \right)^* e^{-in\varphi} d\varphi = 2\pi \delta_{m,n} \Rightarrow \langle m|n \rangle = \delta_{m,n} \quad (\text{C.1})$$

with normalization factor $N = 1/\sqrt{2\pi}$ and the following matrix elements.

The matrix elements of the differential operator in the rotation energy part of H_R is given by

$$\langle m | \partial^2 / \partial\varphi^2 | n \rangle = N^2 \int_{-\pi}^{\pi} \left(e^{-im\varphi} \right)^* \frac{\partial^2}{\partial\varphi^2} e^{-in\varphi} d\varphi = -n^2 \delta_{m,n}. \quad (\text{C.2})$$

The following are the off-diagonal, C_3 symmetry-dependent matrix elements

$$\begin{aligned} \langle m | \cos 3\varphi | n \rangle &= N^2 \int_{-\pi}^{\pi} \left(e^{-im\varphi} \right)^* \cos 3\varphi e^{-in\varphi} d\varphi = \\ &= \frac{1}{2} (\delta_{m,n-3} + \delta_{m,n+3}). \end{aligned} \quad (\text{C.3})$$

The only difference for the C_2 case is the modified form of the above integral as follows:

$$\begin{aligned} \langle m | \cos 2\varphi | n \rangle &= N^2 \int_{-\pi}^{\pi} \left(e^{-im\varphi} \right)^* \cos 2\varphi e^{-in\varphi} d\varphi = \\ &= \frac{1}{2} (\delta_{m,n-2} + \delta_{m,n+2}). \end{aligned} \quad (\text{C.4})$$

Some additional symmetry related details are discussed in the end of this section.

In the above given exponential basis set, the Hamiltonian matrix H_R in Eq. (A.9) with the simple C_3 potential $V(\varphi)$ in Eq. (6) is found to be block diagonal. In fact, three separate banded tridiagonal matrices, one of A and two of E symmetry, were obtained. By increasing the dimension of the matrix to at least 60×60 overall, an acceptable convergence of the eigenvalues was obtained. The tunneling frequency of the ground torsional level is the difference between the average $E_E = (E_a + E_b)/2$ of the minimum degenerate eigenvalues of the E block minus the minimum non-degenerate eigenvalue E_A of the A block. The computation of the tunneling frequency was repeated as a function of the potential barrier V_3 and the C_3 rotational constant $B = 6.752$ K. For the deuterated methyl, half of this value for the rotational constant was used.

On the contrary, the in plane C_2 rotation of methyl requires double these values as rotational constants. This is because the perpendicular moment of inertia of a symmetric top disk is half the parallel value.

Further, the potential energy function in Eq. (13) is different in the simpler C_2 tunneling case compared to C_3 . The Hamiltonian matrix in the C_2 case is blocked in two banded tridiagonal matrices, instead of three, one corresponding to the totally symmetric A and the other to the anti-symmetric B irreducible representations of the Abelian and cyclic C_2 group.

Notice that the above numerical method is flexible in another way, allowing the possibility of involving almost arbitrarily realistic potentials. However, in some of these more complex systems the simplifying block structure of the Hamiltonian matrix as for the above simple C_3 and C_2 potentials may not be possible.

Another advantage of the above numerical treatment is that the higher than the ground level tunneling frequencies can also easily be obtained, because all the higher level eigenvalues of the above Hamiltonian are available by the identical diagonalizing procedure.

The Hamiltonian matrix is in fact of infinite dimensions as $n \rightarrow \infty$ in the basis set $\{|n\rangle : n \in \mathbb{Z}\}$. Therefore, in the computations the matrix dimensions had to be increased until convergence of the eigenvalues was obtained. Except for the matrix dimension dependent convergence procedure, for high potential barriers the tunneling frequency is finally computed as the difference of two very small numbers leading in an all greater numerical uncertainty. Both the above error sources were most serious for deuteron computations as observed in the erroneous flattening of the numerical tunneling data of deuteron at the high V_3 range of Fig. 6(a).

Acknowledgments

N.P.B. is thankful to professor Nikolaos Kyrtziz for assistance in certain numerical methods necessary for the best approach for the presentation of some parts in this work. Yu.A.D. and I.A.Z. acknowledge support of the Russian Foundation for Basic Research (RFBR), research project 16-02-00127a, for the experimental part of the study.

1. V.G. Manzhelii and Yu.A. Freiman, *Physics of Cryocrystals*, AIP, New York (1997).
2. Yu.A. Dmitriev, V.D. Melnikov, K.G. Styrov, and M.A. Tumanova, *Physica B* **449**, 25 (2014).
3. Yu.A. Dmitriev, V.D. Melnikov, K.G. Styrov, and N.P. Benetis, *Physica B* **458**, 44 (2015).
4. Yu.A. Dmitriev, I.A. Zelenetckii, and N.P. Benetis, *Physica B* **537**, 51 (2018).
5. N.V. Krainyukova, B. Kuchta, *J. Low Temp. Phys.* **187**, 148 (2017).
6. V.V. Danchuk, A.A. Solodovnik, M.A. Strzhemechny, *Fiz. Nizk. Temp.* **33**, 783 (2007) [*Low Temp. Phys.* **33**, 600 (2007)].

7. Yu.A. Dmitriev, *Fiz. Nizk. Temp.* **34**, 95 (2008) [*Low Temp. Phys.* **34**, 75 (2008)].
8. T. Kiljunen, E. Popov, H. Kunttu, and J. Eloranta, *J. Chem. Phys.* **130**, 164504 (2009).
9. B.H. Bransden and C.J. Joachain, *Physics of Atoms and Molecules*, Longman Scientific and Technical, New York (1983). p. 455.
10. E.O. Stejskal and H.S. Gutowsky, *J. Chem. Phys.* **28**, 388 (1958).
11. T. Yamada, K. Komaguchi, M. Shiotani, N.P. Benetis, and A. Sørnes, *J. Phys. Chem. A* **103**, 4823 (1999).
12. Yu.A. Dmitriev and N.P. Benetis, *J. Phys. Chem. A* **114**, 10732 (2010).
13. N.P. Benetis, Yu. Dmitriev, F. Mocci, and A. Laaksonen, *J. Phys. Chem. A* **119**, 9385 (2015).
14. T. Kiljunen, E. Popov, H. Kunttu, and J. Eloranta, *J. Phys. Chem. A* **114**, 4770 (2010).
15. Yu.A. Dmitriev, G. Buscarino, and N.P. Benetis, *J. Phys. Chem. A* **120**, 6155 (2016).
16. S.N. Foner, E.L. Cochran, V.A. Bowers, and C.K. Jen, *Phys. Rev. Lett.* **1**, 91 (1958).
17. H.M. McConnell, *J. Chem. Phys.* **29**, 1422 (1958).
18. Yu.A. Dmitriev, *Physica B* **352**, 383 (2004).
19. N.P. Benetis and Yu.A. Dmitriev, *J. Phys.: Condens. Matter* **21**, 103201 (2009).
20. Yu.A. Dmitriev, V.D. Melnikov, K.G. Styrov, and M.A. Tumanova, *Physica B* **440**, 104 (2014).
21. EASYSPIN, free Matlab software written by S. Stoll, <http://www.easyspin.org/>. Accessed August 26, 2016.
22. F.J. Adrian, *J. Chem. Phys.* **32**, 972 (1960).
23. E.P. Kirilina, S.A. Dzuba, A.G. Maryasov, and Yu.D. Tsvetkov, *Appl. Magn. Reson.* **21**, 203 (2001).
24. E. Popov, T. Kiljunen, H. Kunttu, and J. Eloranta, *J. Chem. Phys.* **126**, 134504 (2007).
25. A.K. Vorobiev and N.A. Chernova, *Simulation of Rigid-Limit Slow-Motion EPR Spectra for Extraction of Quantitative Dynamic and Orientational Information*, A.I. Kokorin (ed.), Intech, 2012; 10.5772/74052) Chap. 3.
26. Yu.A. Dmitriev, *Fiz. Nizk. Temp.* **33**, 661 (2007) [*Low Temp. Phys.* **33**, 493 (2007)].
27. E.Y. Misochko, V.A. Benderskii, A.U. Goldschleger, A.V. Akimov, A.V. Benderskii, and C.A. Wight, *J. Chem. Phys.* **106**, 3146 (1997).
28. K.-P. Dinse, *Phys. Chem. Chem. Phys.* **4**, 5442 (2002).
29. S. Goshen, M. Friedman, R. Thieberger, and J.A. Weil, *J. Chem. Phys.* **79**, 4363 (1983).
30. E. Ley-Koo and S. Rubinstein, *J. Chem. Phys.* **73**, 887 (1980).
31. K. Prassides, T.J.S. Dennis, C. Christides, E. Roduner, H.W. Kroto, R. Taylor, and D.R.M. Walton, *J. Phys. Chem.* **96**, 10600 (1992).
32. W. Press, *Single-Particle Rotations in Molecular Crystals*, Springer Trends in Modern Physics, Springer Verlag, Berlin (1981), Vol. 92.
33. I.N. Levine, *Quantum Chemistry*, 2nd ed., Allyn and Bacon, Inc. Boston (1974), p. 158.
34. H.C. Box, E.E. Budzinski, and W.R. Potter, *J. Chem. Phys.* **61**, 1136 (1974).
35. F. Bonon, M. Brustolon, A.L. Maniero, and U. Segre, *Chem. Phys.* **161**, 257 (1992).
36. A.R. Sørnes and N.P. Benetis, *Chem. Phys.* **226**, 151 (1998).
37. C.L. Gardner and E.J. Casey, *Can. J. Chem.* **46**, 207 (1968).
38. M. Prager and A. Heidemann, *Chem. Rev.* **97**, 2933 (1997).

Низькотемпературне тунелювання СН₃ квантового ротора в ван-дер-ваальсових твердих тілах

Nikolas P. Benetis, Ilia A. Zelenetckii,
and Yuriy A. Dmitriev

На основі вимірюваних експериментальних спектрів ЕПР представлено аналіз квантових ефектів, пов'язаних з тунелюванням метильних радикалів, захоплених в твердих газах. Отримано аналітичні вирази для частоти тунелювання метильного радикала навколо осей симетрії з використанням поліномів Ерміта. Ці результати порівнюються з чисельним розрахунком і з даними, отриманими моделюванням експериментальних спектрів ЕПР. Встановлено, зокрема, що спектри ЕПР Х-діапазону демонструють лише залишкову анізотропію, що означає усереднення анізотропії навіть при найнижчих температурах в експерименті. Моделювання спектрів ЕПР з урахуванням динаміки обертового руху використано для коректного отримання величин потенційних бар'єрів та частот тунелювання. Частоти тунелювання, які визначаються як величини розщеплення між A та E обертовими рівнями при наявності модельного C_3 потенціалу та періодичних граничних умов, розраховано та співвіднесено зі зміною форми спектра ЕПР. Також вивчено тунелювання радикала навколо осей C_2 , що лежать в площині симетрії радикала. Представлено порівняння C_2 та C_3 обертань для протонованих й дейтерованих метильних радикалів.

Ключові слова: тверді гази, метильне обертове тунелювання, аналітична частота тунелювання, частота тунелювання в залежності від перешкоджаючих бар'єрів.

Низкотемпературное тунелирование СН₃ квантового ротора в ван-дер-ваальсовых твердых телах

Nikolas P. Benetis, Ilia A. Zelenetckii,
and Yuriy A. Dmitriev

На основе измеренных экспериментальных спектров ЭПР представлен анализ квантовых эффектов, связанных с тунелированием метильных радикалов, захваченных в твердых газах. Получены аналитические выражения для частоты тунелирования метильного радикала вокруг осей симметрии с использованием полиномов Эрмита. Эти результаты сравни-

ваются с численным расчетом и с данными, полученными моделированием экспериментальных спектров ЭПР. Установлено, в частности, что спектры ЭПР X-диапазона демонстрируют лишь остаточную анизотропию, что означает усреднение анизотропии даже при самых низких температурах в эксперименте. Моделирование спектров ЭПР с учетом динамики вращательного движения использовано для корректного получения величин потенциальных барьеров и частот туннелирования. Частоты туннелирования, определяемые как величины расщепления между A и E вращательными уровнями при наличии модельного C_3 потенциала и периодиче-

ских граничных условий, были рассчитаны и соотнесены с изменением формы спектра ЭПР. Также изучено туннелирование радикала вокруг осей C_2 , лежащих в плоскости симметрии радикала. Представлено сравнение C_2 и C_3 вращений для протонированных и дейтерированных метильных радикалов.

Ключевые слова: твердые газы, метильное вращательное туннелирование, аналитическая частота туннелирования, частота туннелирования в зависимости от препятствующих барьеров.